

# Stress-Assisted Thermal Diffusion Barrier Breakdown in Ion Beam Deposited Cu/W Nano-Multilayers on Si Substrate Observed by *in Situ* GISAXS and Transmission EDX

León Romano Brandt,\* Enrico Salvati, Didier Wermeille, Chrysanthi Papadaki, Eric Le Bourhis, and Alexander M. Korsunsky

Cite This: *ACS Appl. Mater. Interfaces* 2021, 13, 6795–6804

Read Online

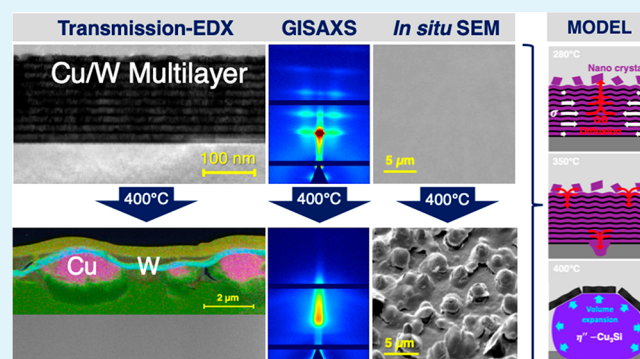
ACCESS |

Metrics & More

Article Recommendations

**ABSTRACT:** The thermal stability of Cu/W nano-multilayers deposited on a Si substrate using ion beam deposition was analyzed *in situ* by GISAXS and transmission EDX—a combination of methods permitting the observation of diffusion processes within buried layers. Further supporting techniques such as XRR, TEM, WAXS, and AFM were employed to develop an extensive microstructural understanding of the multilayer before and during heating. It was found that the pronounced in-plane compressive residual stress and defect population induced by ion beam deposition result in low thermal stability driven by thermally activated self-interstitial and vacancy diffusion, ultimately leading to complete degradation of the layered structure at moderate temperatures. The formation of Cu protrusions was observed, and a model was formulated for stress-assisted Cu diffusion driven by Coble creep along W grain boundaries, along with the interaction with Si substrate, which showed excellent agreement with the observed experimental data. The model provided the explanation for the experimentally observed strong correlation between thin film deposition conditions, microstructural properties, and low thermal stability that can be applied to other multilayer systems.

**KEYWORDS:** nano-multilayer, residual stress, thermal diffusion, GISAXS, copper/tungsten



## 1. INTRODUCTION

Thermal diffusion in nanostructured metallic multilayers is governed by a multitude of interlinked material properties that arise as a consequence of deposition technique and parameters.<sup>1</sup> Among these properties are preferred crystal orientation (texture), grain size and shape, residual stress, density, and defect structure but also the individual layer thickness determining the volume fraction of the material at or near interfaces. In this context Cu/W nano-multilayers (NMLs) on Si substrate are of particular interest due to their mutual immiscibility and resulting clear phase separation. In micro- and nanotechnology applications, tungsten is employed as a diffusion barrier between Si and Cu.<sup>2</sup> Cu/W multilayer coatings are further investigated as radiation-tolerant coatings and heat sinks in plasma-facing components<sup>3</sup> because of the large number of grain boundaries and layer interfaces, which serve as a point defect sink.<sup>4</sup> For this safety-critical field of application a detailed understanding of the thermal diffusion and degradation mechanisms at elevated temperatures is of utmost importance.

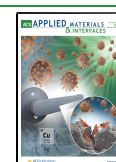
The combination of Cu and W, however, is prone to degradation caused by environmental influences, such as elevated temperatures, oxygen, and electromagnetic radiation. While other material combinations such as complex iron oxides exhibit a higher thermal stability,<sup>5,6</sup> Cu/W multilayer systems exhibit an abrupt structural breakdown at elevated temperatures, which results in the degradation of the layered structure.

Various aspects of this breakdown have been discussed in the literature, while the key elements of understanding the dynamics of inter- and intralayer nanoscale diffusion remain fragmented or lacking. A particularly detailed study of nanostructural transformations within Cu/W NML systems at elevated temperatures was presented by Cancellieri et

Received: October 26, 2020

Accepted: January 22, 2021

Published: January 28, 2021



al.,<sup>7–10</sup> according to which degradation can be subdivided into the following key stages: after the stress-driven formation of Cu nanocrystals at the sample surface at  $T > 400$  °C and a shape change of these particles at  $T > 600$  °C, Cu is reinserted to the multilayer structure at  $T > 700$  °C, resulting in a Cu/W nanocomposite structure. The driving force underlying the NML transformation was identified with the reduction of Gibbs free energy by the minimization of internal interfaces. A model for determining the grain boundary diffusion coefficient for Cu along W grains depending on the residual stress state in W layers presented in ref 10 showed that compressive residual stress increases the barrier to diffusion. Further to the above-described findings involving mostly vertical grain boundary diffusion, *in situ* micropillar compression of Cu/TiN multilayers at ambient and elevated temperatures reported in ref 11 revealed in-plane Cu transport, before coalescence into microcrystals at micropillar sides. The size of these crystals was reported to be independent of the layer thickness. The observed stress-assisted diffusional flow was explained by using a Coble creep model, which links the material strain rate with stress and temperature.<sup>12</sup>

This previous work, however, was mostly limited to sample surface observations during heating, while diffusion phenomena within the sample preceding degradation could not be observed in this way. To overcome this issue, we present an extensive multitechnique analysis of the diffusion and degradation in ion beam deposited (IBD) Cu/W NMLs on a Si substrate, combining large scale averaging techniques such as synchrotron *in situ* X-ray reflectometry (XRR), *in situ* grazing-incidence small-angle X-ray scattering (GISAXS), and wide-angle X-ray scattering (WAXS) with locally probing techniques such as transmission electron microscopy (TEM) imaging, energy-dispersive X-ray spectroscopy (EDX) analysis, and atomic force microscopy (AFM). This combination of methods permits the observation of diffusion mechanisms within and between buried layers of nanostructured coatings before any changes become apparent at the sample surface.

In the present article, we use the obtained experimental insights into the as-deposited and temperature-dependent properties of the sample to reveal how the high kinetic energy of sputtered particles during ion beam deposition results in a complex in-plane residual stress state, pronounced defect structure, and columnar grain morphology. At moderately elevated temperature, the combination of highly compressive residual stress and low thermal activation energy for defect diffusion results in a density decrease. Low-temperature Coble creep and diffusional Cu transport are well described by the analytical expressions that capture the dependence on Cu and W stresses. It was found that the stress-assisted Cu diffusion along W grain boundaries toward the Si substrate results in the formation of copper silicate accompanied by rapid volumetric expansion, ultimately resulting in the observed large-scale morphological multilayer transformation.

## 2. MATERIALS AND METHODS

**2.1. Ion Beam Deposition.** The microstructure of thin films and coatings is determined by the chosen deposition technique and the associated deposition parameters<sup>13–15</sup> as well as postdeposition thermal annealing.<sup>16</sup> While a wide range of deposition techniques are available, IBD was used in this study for the manufacture of multilayer coatings with precise layer thickness control. Ten bilayers of Cu/W were deposited onto 600  $\mu\text{m}$  single crystalline Si wafers obtained from an industrial source with [001] orientation, starting with W. The deposition was performed at room temperature by ion

beam sputtering with a focused Ar<sup>+</sup> ion gun at 1.2 keV multicusp radio-frequency source in a NORDIKO-3000 system.<sup>17</sup> During film growth the ion gun was supplied with constant radio frequency power of 165 W and constant Ar flux of 10 standard cubic centimeters per minute (sccm). The 150 mm diameter targets were sputtered for 10 min, allowing both ion gun stabilization and target pollution cleaning caused by a vacuum break. The ion gun axis was inclined at 45° to the normal of the surface target while the sample surface was parallel to the target plane. The sputtering chamber was pumped down to a base pressure of  $2 \times 10^{-6}$  Pa while the working pressure during film growth was  $\sim 10^{-2}$  Pa. Substrates were preliminarily cleaned with acetone and ethanol and finally dried with an argon gas jet prior to their introduction in the deposition chamber.

**2.2. In Situ X-ray Reflectivity (XRR) Measurements.** To quantify the thickness, roughness, and density evolution of the Cu/W NML at different temperatures, XRR measurements were performed at the BM28 (XMaS) beamline at the European Synchrotron Radiation Facility (ESRF, Grenoble, France). A photon energy of 12.4 keV and beam size of  $0.5 \times 0.2$  mm<sup>2</sup> were chosen. The sample was attached to an 8 mm diameter heater with a PEEK lid by using ceramic adhesive, which was then mounted onto a diffractometer. The heater remained under high vacuum throughout the experiment to avoid sample oxidation. Data collection in a  $2\theta$  range between 0° and 6° was performed at room temperature by using an avalanche photodiode (APD) mounted onto a KF16 flange, followed by one scan at 250 °C. GenX software<sup>18</sup> was used to fit a sample model matching the experimental XRR data and extract the sample parameters at both temperatures.

**2.3. Wide-Angle X-ray Scattering (WAXS).** WAXS patterns in reflection geometry at an incidence angle of 1° with respect to the sample surface were acquired at Diamond Light Source synchrotron Beamline B16 (Didcot, UK) at a beam energy of 18 keV and a beam size of  $250 \times 250$   $\mu\text{m}^2$  by using an Image Star 9000 detector. A sample–detector distance of 66 mm was determined from LaB<sub>6</sub> standard calibration using DAWN software package.<sup>19</sup>

**2.4. In Situ Grazing-Incidence Small-Angle X-ray Scattering (GISAXS) Measurements.** GISAXS is a surface and interface scattering technique that is ideally suited to detect nanoscale periodic features buried within or present on the surface of samples.<sup>20</sup> Because of the very shallow angle of incidence between the beam and sample surface, this technique provides large scale averaged geometric distribution statistics. Temperature-dependent GISAXS patterns during a single heat ramp from 30 to 400 °C were acquired in steps of 10 °C at the BM28 beamline at ESRF. An incidence angle slightly above the conventional GISAXS range (0.05° and 0.5°) of 0.66° was chosen, as it revealed additional lateral and vertical roughness correlation information compared to shallower angles at which the GISAXS pattern was averaged to one large feature without distinct layer separation. The sample environment was identical with the one used for the XRR analysis. An X-ray photon energy of 8 keV with a beam size of  $100 \times 80$   $\mu\text{m}^2$  was chosen to achieve the best possible resolution of the GISAXS patterns on the detector. A PILATUS3 300K area detector with a pixel size of  $172 \times 172$   $\mu\text{m}^2$ , and a resolution of  $487 \times 619$  pixels split into three detector modules was used. A sample–detector distance of 1.56 m was determined by using a AgBh standard calibration sample, followed by analysis in the DAWN software package,<sup>19</sup> which was used to simulate and match the experimentally obtained GISAXS patterns.<sup>21,22</sup>

**2.5. Transmission Electron Microscopy (TEM).** TEM lamellas of a pristine sample and the sample used for the *in situ* GISAXS experiment were extracted and thinned by using a Tescan Lyra3 focused ion beam (FIB) scanning electron microscope (SEM). The lamellas were sectioned by using Ga FIB at a voltage of 30 kV and a beam current of 11 nA, followed by fine polishing and thinning at 0.2 nA beam current. TEM images were acquired at an electron beam energy of 200 keV by using a JEOL JEM-2100 TEM at the Research Complex at Harwell (RCaH, Harwell, UK). In addition, scanning transmission electron microscopy (STEM) on the sample obtained from the GISAXS experiment was combined with transmission energy-dispersive X-ray spectroscopy (t-EDX) inside the Tescan

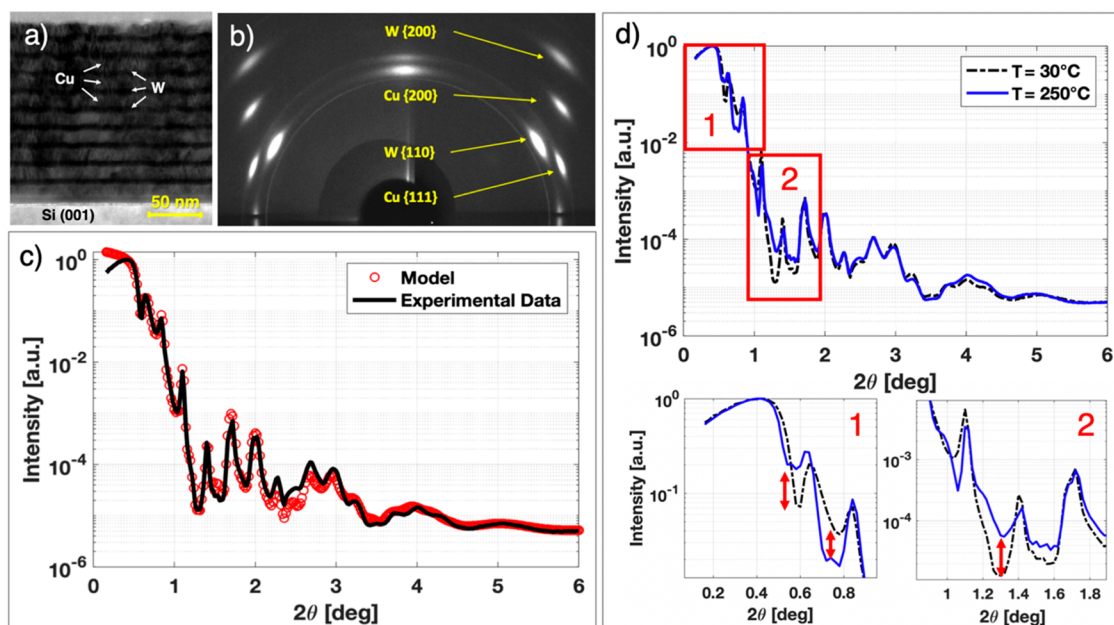


**Figure 1.** (a) Cross-sectional TEM image of the Cu/W nano-multilayer showing the Si substrate and individual Cu (bright) and W (dark) layers. (b) Debye–Scherrer rings of NML with identified reflections indicating highly textured material. (c) Experimental XRR profile (black line) and simulated model (red circles). (d) XRR profile before (black dashed line) and after heating (blue continuous line).

Lyra3 FIB-SEM at an electron beam energy of 20 keV and a working distance of 5 mm, which enabled the local identification of materials based on their characteristic X-ray emission energy at a resolution of  $40 \times 40 \text{ nm}^2$ .

**2.6. Atomic Force Microscopy (AFM).** AFM measurements of the Cu/W NML surface in the as-deposited state and after *in situ* GISAXS heating were acquired at the Laboratory for In Situ Microscopy (LIMA, Department of Engineering Science, University of Oxford) by using a Veeco Dimension 3100 in tapping mode. A surface area of  $0.6 \times 0.6 \mu\text{m}^2$  was scanned for the sample in the reference state, while a map of the surface area of  $5 \times 5 \mu\text{m}^2$  was acquired for the heated sample to capture the newly formed large surface features. ProfilomOnline<sup>23</sup> was used for AFM data processing and rendering.

**2.7. In Situ SEMs Heating.** Finally, to enable sample surface observations during heating, *in situ* SEM analysis of a Cu/W NML was performed using a Zeiss Evo LS15 SEM in combination with the heating module of a 5 kN tensile stage (Kammrath & Weiss, Germany). The multilayer sample was placed on the surface of the heating module, which was then heated in a stepwise fashion from room temperature (RT) up to 400 °C, while SEM frames were acquired. The working distance and beam energy were 20 mm and 10 keV, respectively.

### 3. RESULTS AND DISCUSSION

**3.1. Reference State Characterization.** Prior to studying the thermal stability of the Cu/W NMLs, TEM and XRD based characterization of as-deposited samples was performed to determine the layer thickness, density, and texture. The TEM image in Figure 1a shows 10 bilayers of Cu and W on Si substrate with increasing layer waviness toward the sample surface. This phenomenon has been observed and described in the past and can largely be attributed to columnar growth during energetic film deposition. A formula for calculating the wavelength of the oscillation  $D = 3H + 7 \text{ nm}$  presented in ref 24 based on the thickness of the thicker layer  $H$  returned an estimated wavelength of 46 nm for  $H_{\text{Cu}} = 13 \text{ nm}$ , as estimated from TEM images. This estimate showed excellent agreement with TEM observations and indicates the presence of

cylindrical columnar morphology with a diameter of around 46 nm.

Further to the direct cross-sectional TEM observations, WAXS data shown in Figure 1b were used for phase identification and texture analysis. Face-centered-cubic (FCC) Cu with {111} and {200} crystallographic orientations was confirmed from Debye–Scherrer rings, while the body-centered-cubic (BCC)  $\alpha$ -W phase with {110} and {200} crystallographic orientations was present. Pronounced fiber texture was present in all phases, as can be seen from the strong azimuthal intensity variations of the Debye–Scherrer rings shown in Figure 1b. It was previously shown that the presence of strong texture in magnetron sputtered Cu/W NMLs at low Ar pressure coexists with in-plane compressive residual stresses and increased thermal diffusivity.<sup>25</sup> Because the Ar pressure during IBD was around 1 order of magnitude below the magnetron sputtering chamber pressure, a reduced level of interaction between highly energetic sputtered metal atoms and Ar atoms inside the deposition chamber can be assumed. A previous comparative study confirmed this assumption<sup>26</sup> by showing that while magnetron sputter deposition emits particles in an energy range between 1 and 100 eV when reaching the sample surface, ion beam deposited particles can reach up to 1000 eV, thus enabling the implantation of self-interstitials in Cu<sup>27</sup> when considering the kinetic particle energy of around 20 eV<sup>28</sup> required for their formation. As a result, self-interstitial formation and “atomic peening”<sup>29</sup> as well as atom insertion into grain boundaries<sup>30</sup> result in highly densified Cu and W layers under compressive residual stress. Indeed, the residual stress state of identical Cu/W NML systems deposited by using the identical deposition system was evaluated in the past<sup>31</sup> and found to be  $-6.6 \text{ GPa}$  for W and  $-0.4 \text{ GPa}$  for Cu, as determined by  $\sin^2(\Psi)$  analysis. The average film stress was determined by substrate curvature analysis and was found to be  $-1.0 \text{ GPa}$ .<sup>31</sup> While a W stress of  $-6.6 \text{ GPa}$  seems high at first, a recent study has shown that nanocrystalline tungsten with a crystal size of 10 nm can



sustain considerably larger compressive stresses.<sup>32</sup> The depth profile of the in-plane stress distribution within the Cu/W NML on Si substrate can be assumed to be near 0 GPa at the sample surface, while a pronounced stress peak near the NML–substrate interface is present.<sup>33</sup>

The X-ray reflectometry profile of the Cu/W NML in reference state at room temperature is shown in Figure 1c alongside the fitted profile using GenX software. The obtained average layer parameters listed in Table 1 show the thickness

**Table 1. Cu/W NML Average Layer Thickness, Roughness, and Density at 30 °C vs 250 °C as Obtained from XRR Profile Fitting**

sample temperature	30 °C	250 °C
W thickness [nm]	5.86 ± 0.01	5.25 ± 0.07
W roughness [nm]	1.07 ± 0.001	1.65 ± 0.01
Cu thickness [nm]	12.97 ± 0.02	13.59 ± 0.04
Cu roughness [nm]	1.35 ± 0.002	3.44 ± 0.04
W density [g/cm <sup>3</sup> ]	18.13 ± 0.01 (94% bulk)	16.94 ± 0.14 (88% bulk)
Cu density [g/cm <sup>3</sup> ]	8.43 ± 0.04 (94% bulk)	7.92 ± 0.06 (88% bulk)
Si roughness [nm]	0.28 ± 0.02	1.27 ± 0.21

and roughness of Cu and W layers. Furthermore, a high relative layer density found in both nanocrystalline Cu and W reached 94% of their bulk material density,<sup>34</sup> which further provides supporting experimental evidence for the presence of self-interstitials arising from the above-described layer densification mechanisms, as well as vacancy defects, which lower the overall density below single crystal level.

### 3.2. Structural Evolution upon Thermal Treatment.

XRR intensity profiles were further acquired at 250 °C, as shown in comparison with the reference scans in Figure 1d. While the overall intensity versus  $2\theta$  distribution is similar to

the reference state, distinct differences are identifiable in the regions labeled “1” and “2”. Amplitude changes revealing differences in layer density and layer roughness<sup>35</sup> are highlighted by red arrows in the magnified regions shown underneath the graph. The layer thickness, density, and roughness at 250 °C for both Cu and W are compared with the reference state in Table 1. A significant decrease in layer density by 6% upon heating was observed for both materials, while an increase in layer roughness by a factor of 1.5 and 2.5 was observed for W and Cu, respectively. The layer thickness data in Table 1 reveal that the overall thickness of Cu and W bilayer remained constant at 18.8 nm between XRR scans. At the same time, the Cu layer thickness increased by 0.6 nm, while the W layer thickness decreased by the same amount. This clearly points at the consequence of interface diffusion activity between Cu and W layers. Within the two-component GENX model, the newly formed boundary layer was assigned to the Cu layer, indicating that the boundary layer density was closer to that of Cu than that of W, corresponding to the diffusion of W atoms into the Cu layer. This process proceeds alongside the observed reduction in W layer density shown in Table 1. Furthermore, while the overall stack thickness was preserved, superficial Cu “islands” appeared as a consequence of Cu atomic transport toward the multilayer surface between 230 and 250 °C, as shown in Figure 3. Considering the increase in the Cu layer thickness this necessarily leads to the reduction of Cu layer density. This is discussed in further detail in the following section.

One possible driver underlying the diffusion of Cu toward the sample surface which further results in a density decrease is the thermal activation of Cu self-interstitial motion, which was shown to require less thermal energy as compared to vacancy motion.<sup>27,36</sup> Vacancy-interstitial annihilation can further contribute to the volumetric expansion and decrease in

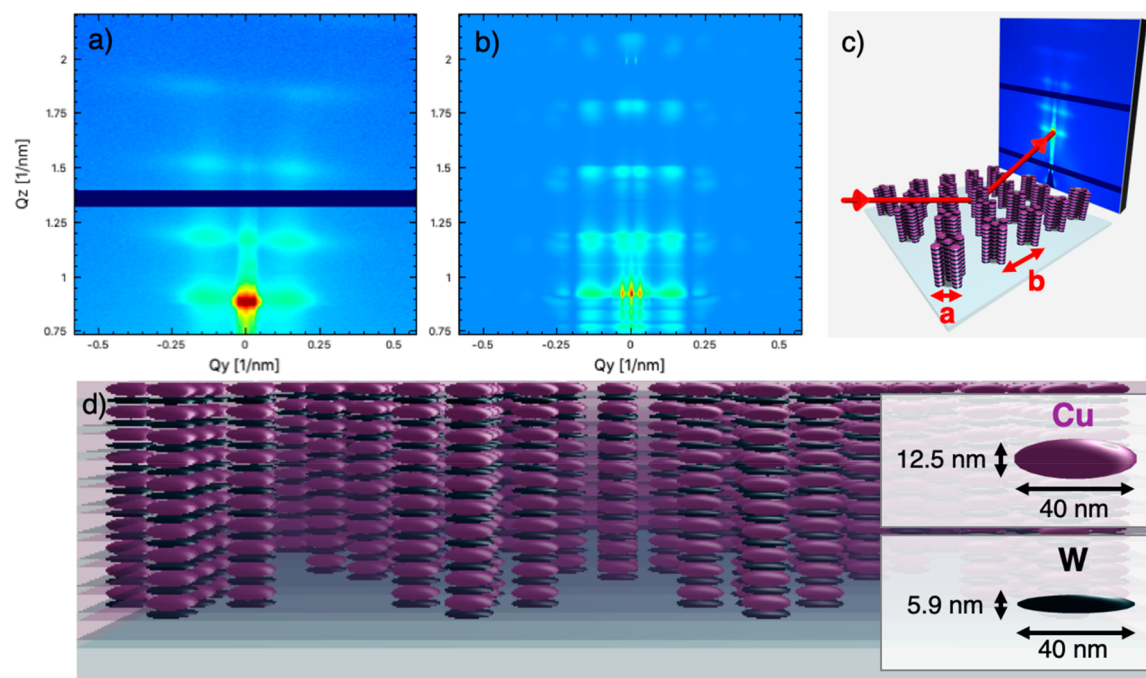


**Figure 2.** (a) GISAXS pattern of Cu/W NML at 30 °C. (b) Simulated Cu/W GISAXS pattern based on BornAgain material model. (c) Overview of BornAgain model and scattering geometry. Cu/W columnar grains are shown on Si substrate, alongside incoming and reflected beam. While the Cu and W particles are embedded in Cu and W layers in the simulation, they have been removed from the illustration for the purpose of visibility. (d) Side view of rendering showing the simulated multilayer microstructure with columnar Cu/W growth. Dimensions are indicated on the right.



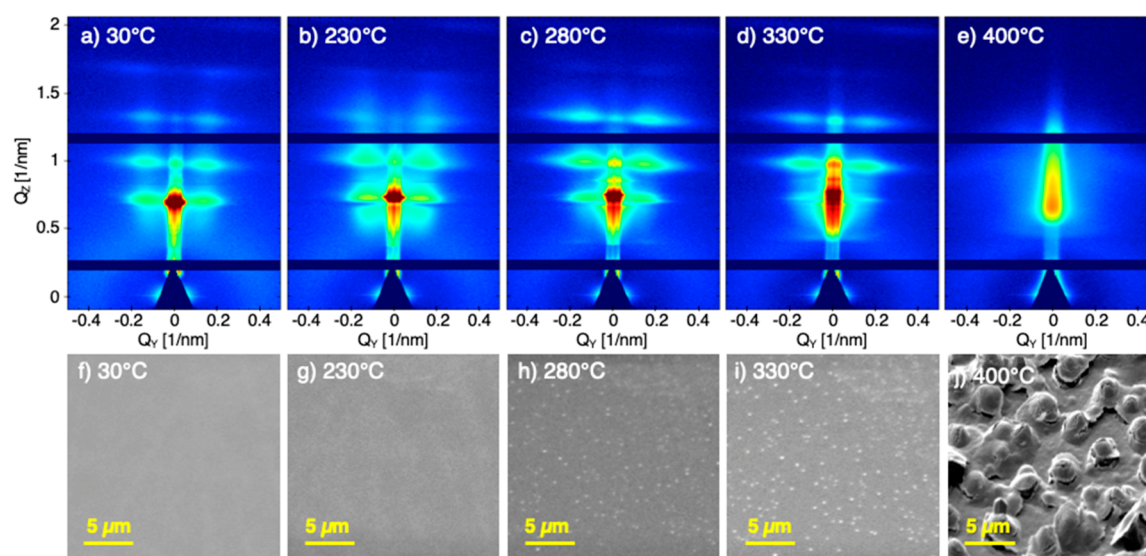


**Figure 3.** (a–e) Temperature-dependent GISAXS patterns. (f–j) *In situ* in-SEM surface observations during temperature increase.

density.<sup>37</sup> These mechanisms, however, can only be speculated on and require further high-resolution TEM analysis. Thermal expansion of the layers, however, was found to have a minimal contribution to the observed changes in layer thickness, with a Cu expansion of 0.39% for a temperature increase of 230 °C, assuming a thermal expansion coefficient of  $\alpha_{\text{Cu}} = 17.7 \times 10^{-6}$  1/K.<sup>38</sup> Considering the lower thermal expansion coefficient of nanocrystalline W with  $\alpha_{\text{W}} = 4.5 \times 10^{-6}$  1/K,<sup>39</sup> the in-plane thermal expansion of Cu is hindered by the W layers, resulting in an increase in in-plane compressive residual stress within Cu layers by around 300 MPa and a decrease in W in-plane residual stress. While the initial grain size of nanocrystalline Cu and W deposited by IBD was found to correspond to the individual layer thickness in previous studies,<sup>31</sup> grain coarsening in nano-multilayers at elevated temperature was identified and described in the literature for comparable systems,<sup>40</sup> thus suggesting that significant grain growth occurred during the thermal annealing of the Cu/W system in this study.

In summary, thermal activation of diffusion processes at 250 °C resulting in measurable microstructural changes in both Cu and W was confirmed experimentally—an activation temperature significantly below other values reported in the literature based on surface observations during heating. Highly compressive in-plane residual stresses and a complex defect structure, both of which were introduced by ion beam deposition, are suggested as underlying reasons alongside thermal diffusion at the layer boundaries.

To gain further insights into the temperature-dependent evolution of the microstructure at higher temperatures, GISAXS patterns were collected between 30 and 400 °C. In its as-deposited state the NML exhibits a periodic vertical GISAXS pattern with a period corresponding to the Cu/W bilayer thickness (Figure 2a). Additional intensity contributions related to reflection and refraction phenomena at interfaces within the multilayer, however, make a detailed analysis of individual peaks challenging. The intensity loss of pattern features along the  $Q_z$  direction is representative of the interface roughness,<sup>41</sup> with a steeper decay toward higher  $Q_z$  representing a higher degree of interface roughness. The specular peak is shown as red dot in the center of the frame at

$Q_y = 0 \text{ nm}^{-1}$  and  $Q_z = 0.825 \text{ nm}^{-1}$ . Distinct lateral peaks are visible at  $Q_y = \pm 0.13 \text{ nm}^{-1}$ , corresponding to a lateral in-plane geometric ordering of 48 nm. This is in strong agreement with the estimated columnar grain diameter of 46 nm based on TEM images. Further in-plane ordering at low  $Q_y$  between  $\pm 0.0265 \text{ nm}^{-1}$  is visible in the pattern center, indicating ordering at larger length scales of  $\geq 237 \text{ nm}$ . Based on this information and combined with the data obtained from XRR fitting, a hierarchical microstructural multilayer model was implemented in the BornAgain software package, as illustrated in Figure 2c showing the experiment geometry and Figure 2d showing the model side view. For this purpose, columnar multilayer morphology was simulated by means of cylindrical layered mesocrystals consisting of alternating 40 nm diameter Cu and W particles with heights of 12.5 and 5.9 nm, respectively, as shown in Figure 2d. The Cu/W particles with an intercolumnar spacing of 48 nm (characteristic length  $a$  in Figure 2c) were embedded in a Cu/W multilayer structure which is indicated by the transparent layers in Figure 2d. To account for the lateral ordering at low  $Q_y$ , the mesocrystals were arranged within the model in a hexagonal grid with a spacing of 237 nm (length  $b$  in Figure 2c). While further model accuracy could be achieved by adding additional mesocrystal clusters with a variation of spacings instead of embedding a single cluster in continuous Cu and W layers, the present simulation delivered excellent agreement with the experimentally obtained GISAXS pattern, as shown in Figure 2b. A smooth and uniform sample surface in the sample reference state was confirmed by *in situ* imaging of the sample surface during heating, as shown in Figure 3f. It was therefore experimentally confirmed that ion beam deposition of Cu/W NMLs results in the formation of columnar grain structures during deposition.

Upon heating, the first changes in the scattering intensity distribution were observed at a temperature of 230 °C, as shown in Figure 3b. Peak blurring along the  $Q_z$  direction was observed, resulting in a decreased vertical spacing between individual peaks, thus indicating an increase in Cu layer thickness and decrease in density, as previously confirmed by XRR at 250 °C. While these changes were observed within buried layers and interfaces, no changes on the sample surface

were identified from *in situ* in-SEM sample heating at the same temperature (Figure 3f–j). In contrast, the formation of randomly spaced surface crystals was observed at  $T = 280\text{ }^{\circ}\text{C}$ , as shown in Figure 3h. The crystal composition was confirmed as pure Cu from EDX spectroscopy. At the same temperature, the GISAXS pattern showed an increase in intensity at higher order  $Q_z$  peaks, indicating an increase in vertical layer correlation, which may be related to changes in layer roughness. Particularly the third-order peak at  $Q_z = 1.35\text{ nm}^{-1}$  notably increased in intensity in addition to feature sharpening. Combined with the observed Cu surface crystal formation, it can be assumed that the Cu atoms released from highly densified nanocrystals during heating that led to a layer thickness increase at  $230\text{ }^{\circ}\text{C}$  started migrating in vertical direction toward the sample surface at  $280\text{ }^{\circ}\text{C}$ . While the origin of the surface crystal Cu could not be attributed to specific layers, nanoscale transport mechanisms described in the literature indicate that they are to a large extent composed of material from buried Cu layers due to the prevailing residual stress state in the sample. Furthermore, a shift of intensity from the lower lateral peaks toward lower  $Q_y$  at the pattern center can be observed, which can be interpreted as a large-scale transformation from a regularly spaced columnar structure toward larger and more randomly spaced and sized objects, for instance by columnar grain coalescence.

**3.3. Diffusion Modeling.** A feasible diffusion mechanism of Cu along W grain boundaries toward the free sample surface has been described recently;<sup>10</sup> however, the observed onset temperature of  $280\text{ }^{\circ}\text{C}$  for surface crystal formation in this study lies significantly below the  $400\text{ }^{\circ}\text{C}$  reported. While the materials and layer thicknesses involved are identical with the literature data, differences in residual stress state and defect structure are the possible drivers underlying the lower thermal stability. While the samples presented in refs 9 and 10 were deposited by using magnetron sputter deposition with a resulting residual stress state of  $-3$  and  $-0.5\text{ GPa}$  compressive residual stress for W and Cu, respectively, IBD employed for the samples presented in this article induces a more pronounced defect structure during deposition as well as a higher level of compressive residual stress. On the basis of previous study, it is known that the in-plane stress gradient along the vertical direction ranges from a stress-free surface layer to a compressive stress peak near the NML–substrate interface.<sup>33</sup> As a consequence, diffusional transport from highly compressive buried Cu layers toward the stress-free surface appears to be the underlying transport mechanism. The diffusion coefficient of Cu atoms along W grain boundaries with account taken of the residual stress in the W layers is expressed in ref 10 as follows:

$$D_b(\sigma) = D_0 e^{(\sigma_{ii,W}\Omega/3RT) - (E_A^*/kT)} \quad (1)$$

with a pre-exponential factor of the self-diffusivity of nanocrystalline Cu  $D_0$ , an in-plane tungsten interlayer first stress invariant of  $\sigma_{ii,W} = \sigma_{11,W} + \sigma_{22,W}$  ( $\sigma_{33} = 0$ ), a diffusion activation volume  $\Omega$ , the Avogadro gas constant  $R$ , temperature  $T$ , a diffusion activation energy  $E_A^*$ , and the Boltzmann constant  $k$ .

Furthermore, micropillar compression of Cu/TiN NMLs at elevated temperatures<sup>11</sup> revealed anomalous plastic flow of Cu alongside a significant reduction in Cu 0.5% yield stress at a temperature of  $200\text{ }^{\circ}\text{C}$  to around  $0.81\text{ GPa}$ . This value lies close to the above-estimated Cu residual stress at  $250\text{ }^{\circ}\text{C}$ ,

indicating that the Cu layer has been compressed beyond yield stress at this point. The observed outflow of Cu from the micropillar boundary was explained by using a Coble creep model depending on the stress state in Cu layers:

$$\frac{d\epsilon}{dt} = \dot{\epsilon} = A_c \frac{\delta'}{d^3} \frac{\sigma_{Cu} V_{Cu}}{kT} D_{GB} \quad (2)$$

with the strain rate  $\dot{\epsilon}$ , a geometric prefactor  $A_c$ , the grain boundary width  $\delta'$ , the layer thickness  $d$ , the Cu atomic volume  $V_{Cu}$ , the residual stress in Cu layers  $\sigma_{Cu} = \sigma_{11} = \sigma_{22}$ , and the diffusion coefficient in the grain boundary  $D_{GB}$ .

The stress-driven Cu diffusion observed in this study appears to be similar to the micropillar compression-induced plastic flow,<sup>11</sup> however, with in-plane compression generated by a combination of residual stress and thermal expansion coefficient mismatch, resulting in vertical diffusion as opposed to vertical nanoindenter driven compression resulting in in-plane plastic flow. Equations 1 and 2 can therefore be combined to obtain a model for the stress-assisted migration of Cu toward the sample surface. While the model in ref 10 focuses on the effect of residual stress in the W interlayer on the diffusion of Cu across this interlayer, the model presented in ref 11 only considers the role of the applied stress on the Cu layer for diffusion analysis. Combining these two models therefore yields a model accounting for the implications of residual stresses in both Cu and W layers and the effect on the material transport toward the sample surface. As a result, an expression describing the residual stress-driven diffusion of in-plane compressed copper in vertical direction across W barrier layers was obtained:

$$\frac{d\epsilon}{dt} = \dot{\epsilon} = A_c \frac{\delta'}{d^3} \frac{\sigma_{Cu} V_{Cu}}{kT} D_0 e^{(\sigma_{ii,W}\Omega/3RT) - (E_A^*/kT)} \quad (3)$$

For further calculation, the parameters shown in Table 2 were employed.

**Table 2. Parameters Used to Calculate Temperature-Dependent Coble Creep Strain Rate**

parameter	value	parameter	value
$D_0$ <sup>42</sup>	$3 \times 10^{-9}\text{ m}^2/\text{s}$	$\delta'$ <sup>11</sup>	$0.5 \times 10^{-10}\text{ m}$
$\sigma_{11,W} = \sigma_{22,W}$	$-6.6 \times 10^9\text{ Pa}$	$d$	$13 \times 10^{-9}\text{ m}$
$\Omega$ <sup>10</sup>	$7.69 \times 10^{-6}\text{ m}^3/\text{mol}$	$\sigma_{Cu}$	$-0.4 \times 10^9\text{ Pa}$
$E_A^*$ <sup>42</sup>	$1.025 \times 10^{-19}\text{ J}$	$V_{Cu}$ <sup>11</sup>	$8.78 \times 10^{-30}\text{ m}^3$
$A_c$ <sup>11</sup>	148		

The resulting temperature-dependent Coble creep strain rate within a Cu layer was calculated and is shown in Figure 4. It becomes apparent that the residual stress state in the Cu layer has a strong effect on the strain rate and thus the nanoscale transport. For a residual stress of  $-0.4\text{ GPa}$  in the Cu layer and  $-6.6\text{ GPa}$  in the W layer, the Coble creep strain rate at  $280\text{ }^{\circ}\text{C}$  was calculated as  $-4.35 \times 10^{-3}\text{ 1/s}$ , which provides a convincing explanation for the observed surface crystal formation temperature.

Subsequently raising the sample temperature to  $330\text{ }^{\circ}\text{C}$  resulted in a further significant intensity shift from  $Q_y = \pm 0.13\text{ nm}^{-1}$  toward the pattern center, indicating the gradual disappearance of lateral ordering and formation of random large-scale structures buried within the multilayer structure, while surface crystals grow further, as shown in Figure 3d,i. The further reduction in lateral peak intensity at  $Q_z = 0.68\text{ nm}^{-1}$  may partly be caused by the obstruction of the exiting X-



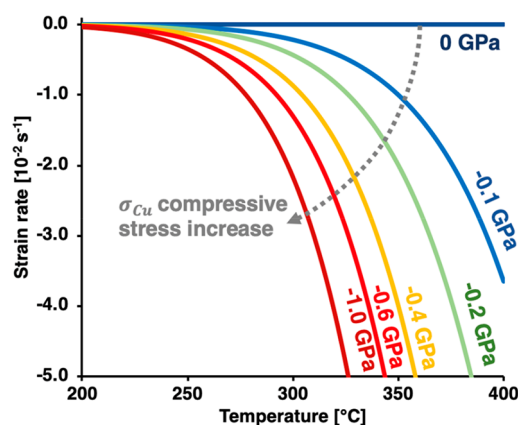


**Figure 4.** Evolution of Cu layer strain rate vs temperature and layer stress.

ray photons by the surface Cu crystals. A significant increase in low- $Q_y$  intensity (red peak) further confirms the transformation from evenly spaced columnar grains toward large-

scale and more random ordering. Finally, increasing the temperature beyond 330 °C resulted in a gradual collapse of the sample nanostructure in both lateral and vertical directions, as shown in the final GISAXS pattern in Figure 3e which shows a single specular peak in the pattern center at 400 °C. Looking at the SEM frame in Figure 3j acquired after heating the sample to 400 °C clearly shows the significant microstructural transformation that has occurred during heating, with spheroidal features being buried underneath a thin surface layer.

To further investigate the composition of these micro-particles and understand the mechanisms leading to their formation, cross-sectional TEM and t-EDX analysis of the sample heated during the GISAXS experiment was carried out. For this purpose, a thin, electron transparent TEM lamella was created by using Ga<sup>+</sup> FIB, as described in the Materials and Methods section. T-EDX on TEM lamellae was used to limit the interaction volume between sample and electron beam, resulting in a significantly improved local resolution. The lamella cross section of the sample after heating is shown in Figure 5. The material map in Figure 5a clearly shows the

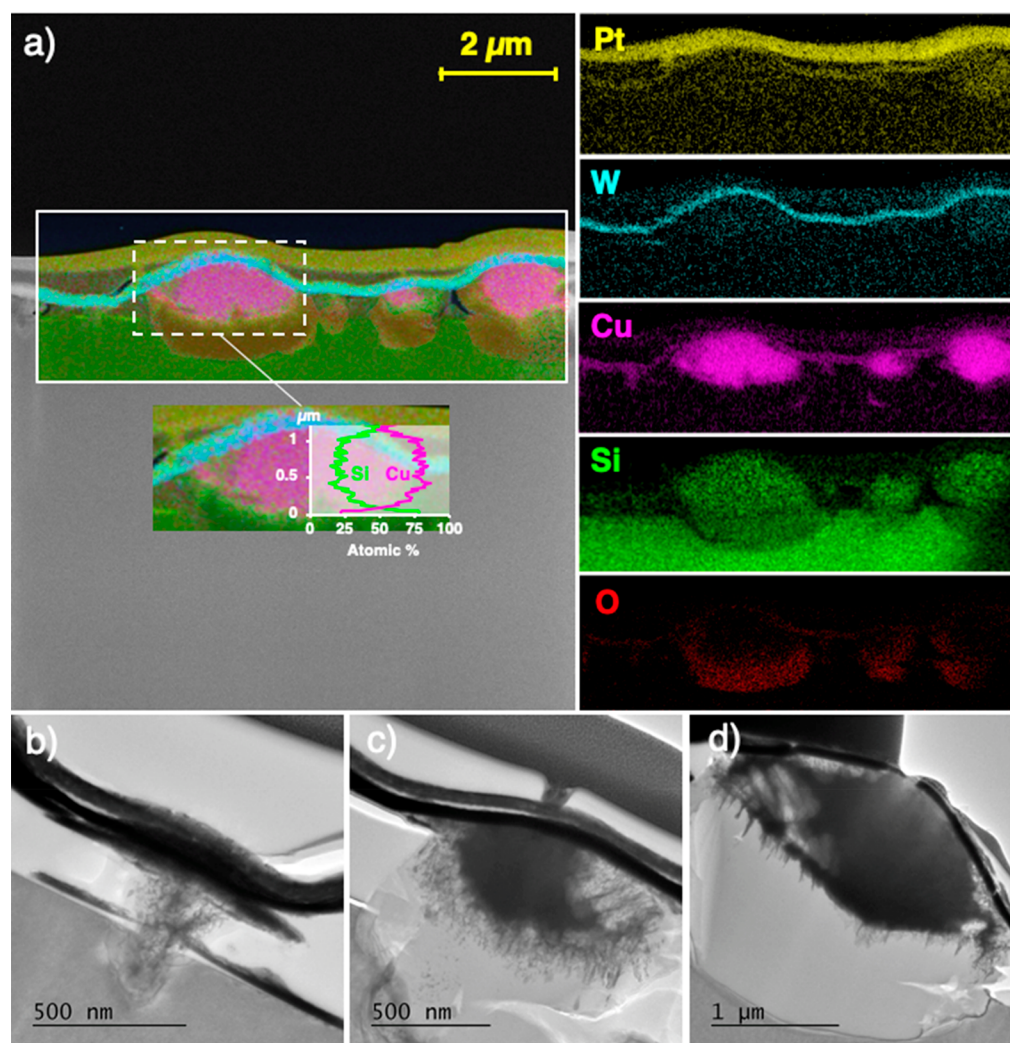


**Figure 5.** Cross-sectional TEM lamella of Cu/W nano-multilayer on Si substrate after heating to 400 °C, showing a full degradation of the layered structure. (a) Left: transmission EDX map showing the material distribution after heating. Local atomic percentage is shown in the detail frame underneath. Right: detailed maps for each element showing the exact local material distribution. (b–d) TEM images of spheroidal particles in different stages of growth from early stage (b) to final particle (d).



significant diffusion driven transformation. The nanostructured Cu layers have coalesced into flat spheroidal microparticles buried underneath a thick tungsten layer. The identified surface Pt layer was deposited prior to lamella cutting for surface protection. The material distribution within the Cu microparticles was identified based on quantitative stoichiometric analysis, as shown in the graph underneath the material map. The particle was composed of 75 atomic % Cu and 25 atomic % Si, indicating the presence of the orthorhombic or tetragonal  $\eta''$ -Cu<sub>3</sub>Si phase, while the presence of the  $\eta$  and  $\eta'$  phases is unlikely due to the higher formation temperature required.<sup>44</sup> TEM images shown in Figure 5b–d show the different stages of Cu<sub>3</sub>Si microparticle formation: Cu penetration across the W diffusion barrier into the Si substrate results in the precipitation of Cu<sub>3</sub>Si, leading to a significant volumetric expansion<sup>45</sup> as can be seen in Figure 5b. A reason for the delayed diffusion of Cu into Si as compared to previously described diffusion toward the free sample surface can be found by looking at the thermal expansion coefficient mismatch between W and Si. Because the W diffusion barrier layer showed excellent adhesion with the Si substrate, W expansion was hindered by interfacial adhesion. While near-surface W layers experienced a decrease in residual stress caused by Cu expansion, the first W layer on Si experienced an increase in compressive residual stress. According to eq 1, this reduces the thermal diffusion significantly, resulting in a delayed nanoscale mass transport at higher temperature range, once the Cu compressive residual stress reaches the threshold value required for diffusion along the highly compressive W grain boundaries. Once Cu diffuses into the substrate, the expanding Cu–Si alloy breaks across the multilayer structure, permitting the absorption of further interlayer Cu, while additional Si from the substrate contributes to particle growth by sustaining the formation of Cu<sub>3</sub>Si (Figure 5c). In the final stage, the multilayer structure has been entirely deprived of Cu, leaving a layered pure W structure on top of the Cu<sub>3</sub>Si particles (Figure 5d). A possibility of increasing the thermal stability of diffusion barriers was identified in recent studies<sup>46,47</sup> by adding a second phase and thus improving the electronic properties of the resulting composite material, which may be used to improve the stability of the W diffusion barrier between Cu and Si. Further to the above-described mechanism of copper–silicate formation, the presence and role of oxygen in the multilayer system were analyzed, as the presence of oxygen anions can lead to a significant change in electronic parameters.<sup>48,49</sup> A substrate surface oxide layer with a SiO<sub>2</sub> thickness of around 0.5 nm originating from room temperature surface oxidation before multilayer deposition was identified based on the TEM image in Figure 1a. While t-EDX confirmed that no oxygen was present in the Cu<sub>3</sub>Si alloy, the formation of SiO<sub>2</sub> areas underneath the copper–silicate protrusions was observed, as can be seen in Figure 5a.

Finally, the described large-scale transformation was confirmed by comparative AFM surface scans performed before and after heating. The scan in reference state shown in Figure 6a shows regular surface peaks with an average spacing of around 50 nm, thus corresponding to the previously determined columnar grain spacing. A large contrast in both shape and size of the objects can be seen in the post heating scan shown in Figure 6b, which confirms the presence of microparticles with a height of around 1  $\mu\text{m}$  and a diameter of around 3  $\mu\text{m}$ .

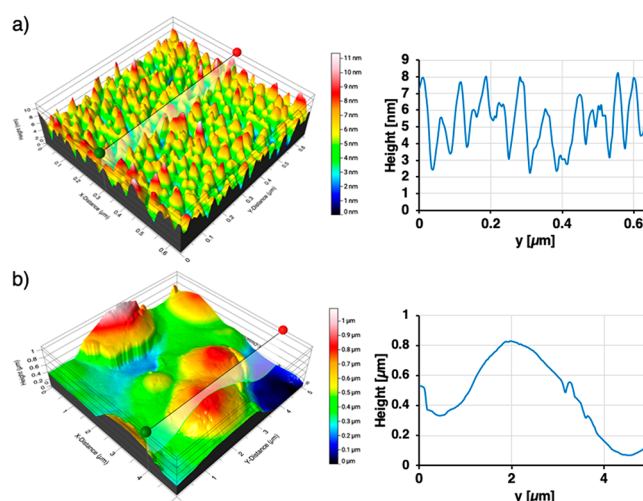


**Figure 6.** AFM scans of the sample surface (a) in reference state and (b) after heating. Line profiles shown on the right are indicated by the black line on the left.

In summary, based on the experimental insights described above, the following degradation mechanism of Cu/W NMLs on Si substrate was identified:

- (1) Ion beam deposition induced vacancy diffusion is activated at  $T > 230\text{ }^{\circ}\text{C}$ , resulting in interface diffusion in between Cu and W layers, Cu layer thickness increase, and W layer decrease as well as roughness increase and density decrease (Figure 7b).
- (2) Additional compressive stress in Cu layers at  $280\text{ }^{\circ}\text{C}$  exceeds the nanocrystalline yield stress. As a consequence, stress-induced Coble creep results in nanoscale Cu diffusion along W grain boundaries toward the sample surface. The formation of Cu nano crystals can be observed on the sample surface (Figure 7c).
- (3) Beyond  $330\text{ }^{\circ}\text{C}$  a large-scale microstructural transformation can be observed: thermally induced stress in the lower Cu layers exceeds the diffusion threshold in the W diffusion barrier. As a consequence, Cu diffuses into Si substrate, resulting in  $\eta''$ -Cu<sub>3</sub>Si formation associated with rapid volumetric expansion, thus breaking down the layered structure, resulting in Cu absorption and complete transformation into  $\eta''$ -Cu<sub>3</sub>Si (Figure 7d,e).

## 4. CONCLUSION

Three key results were presented in this study: First, a novel and powerful combination of advanced experimental methods was employed to obtain temperature-dependent insights into stress and diffusion mechanisms within buried layers of nanostructured materials. Second, the effect of highly energetic particle deposition methods on the thermal stability and residual stress state was discussed before the background of defect formation and diffusion. A clear link between deposition conditions, nanoscale defect structure, and thermal instability was established. Finally, this new understanding was used to develop a detailed description and model of the Coble creep induced strain within Cu layers, resulting in vertical diffusion of Cu across W layers into the Si substrate. It was found that the pronounced compressive residual stresses and defects arising from ion beam deposition contribute to large extent to the degradation of the nanostructured coating through a

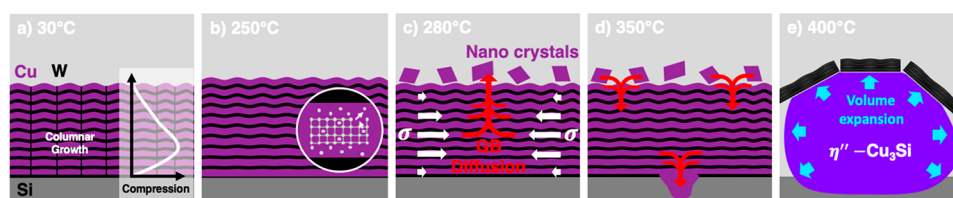


**Figure 7.** Illustration showing the mechanism leading to large-scale microstructural breakdown in Cu/W nano-multilayers on the Si substrate.

mechanism of Cu diffusion into the Si substrate, ultimately resulting in a transformation of nanostructured Cu layers into  $\eta''$ -Cu<sub>3</sub>Si protrusions. Considering the low onset temperature and complex diffusion mechanism underlying structural degradation, the use of pure Cu/W nano-multilayers as radiation-tolerant coating and heat sink in plasma-facing components does not seem suitable, as temperatures are likely to exceed the identified critical diffusion onset temperature of 250 °C. Further investigations into possible stability enhancements of Cu/W nano-multilayers—for instance by introducing stabilizing impurity phases—need to be pursued in future work to unlock enhanced temperature stability, while benefiting of the multilayer capability as point defect sink for radiation damage.

## AUTHOR INFORMATION

### Corresponding Author

**León Romano Brandt** – Multi-Beam Laboratory for Engineering Microscopy, Department of Engineering Science, University of Oxford, Oxford OX1 3PJ, United Kingdom;  
 orcid.org/0000-0002-4195-9993;  
 Email: leon.romanobrandt@eng.ox.ac.uk

### Authors

**Enrico Salvati** – Multi-Beam Laboratory for Engineering Microscopy, Department of Engineering Science, University of Oxford, Oxford OX1 3PJ, United Kingdom; Polytechnic Department of Engineering and Architecture (DPIA), University of Udine, Udine, Italy  
**Didier Wermeille** – XMaS Beamline BM28, European Synchrotron Radiation Facility (ESRF), 38043 Cedex 9 Grenoble, France  
**Chrysanthi Papadaki** – Multi-Beam Laboratory for Engineering Microscopy, Department of Engineering Science, University of Oxford, Oxford OX1 3PJ, United Kingdom  
**Eric Le Bourhis** – Institut P', UPR 3346, CNRS, Université de Poitiers, 86073 Poitiers, France  
**Alexander M. Korsunsky** – Multi-Beam Laboratory for Engineering Microscopy, Department of Engineering Science, University of Oxford, Oxford OX1 3PJ, United Kingdom;  
 orcid.org/0000-0002-3558-5198

Complete contact information is available at:  
<https://pubs.acs.org/10.1021/acsami.0c19173>

### Notes

The authors declare no competing financial interest.

## ACKNOWLEDGMENTS

The authors acknowledge the European Synchrotron Radiation Facility (ESRF) for the allocation of beam time under experiment number 28-01-1208 and Diamond Light Source for allocation of beam time under experiment number MT19192-1. A.M.K. acknowledges funding received from the Engineering

and Physical Sciences Research Council (EPSRC) [EP/682 P005381/1] and [EP/S005072/1]. The authors further thank Mr. Enrique Alabort Martinez for *in situ* operation of in-SEM sample heating stage. We also thank Marzena Tkaczyk (Laboratory for *in situ* microscopy, LIMA, Department of Engineering Science, University of Oxford) for her help with operating the AFM.

## REFERENCES

- (1) Abadias, G.; Chason, E.; Keckes, J.; Sebastiani, M.; Thompson, G. B.; Barthel, E.; Doll, G. L.; Murray, C. E.; Stoessel, C. H.; Martinu, L. Review Article: Stress in thin films and coatings: Current status, challenges, and prospects. *J. Vac. Sci. Technol., A* **2018**, *36*, 020801.
- (2) Chang, K.-M.; Yeh, T.-H.; Deng, I.-C.; Shih, C.-W. Amorphous-like chemical vapor deposited tungsten diffusion barrier for copper metallization and effects of nitrogen addition. *J. Appl. Phys.* **1997**, *82*, 1469.
- (3) Gao, Y.; Yang, T.; Xue, J.; Yan, S.; Zhou, S.; Wang, Y.; Kwok, D. T. K.; Chu, P. K.; Zhang, Y. Radiation tolerance of Cu/W multilayered nanocomposites. *J. Nucl. Mater.* **2011**, *413*, 11–15.
- (4) Ackland, G. Controlling radiation damage. *Science (Washington, DC, U. S.)* **2010**, *327*, 1587–1588.
- (5) Turchenko, V. A.; Trukhanov, A. V.; Bobrikov, I. A.; Trukhanov, S. V.; Balagurov, A. M. Investigation of the crystal and magnetic structures of BaFe<sub>12</sub> - xAlxO<sub>19</sub> solid solutions (x = 0.1–1.2). *Crystallogr. Crystallogr. Rep.* **2015**, *60*, 629–635.
- (6) Kozlovskiy, A. L.; Kenzhina, I. E.; Zdorovets, M. V. FeCo-Fe<sub>2</sub>CoO<sub>4</sub>/Co<sub>3</sub>O<sub>4</sub> nanocomposites: Phase transformations as a result of thermal annealing and practical application in catalysis. *Ceram. Int.* **2020**, *46*, 10262–10269.
- (7) Cancellieri, C.; Moszner, F.; Chiodi, M.; Yoon, S.; Janczak-Rusch, J.; Jeurgens, L. P. H.; Moszner, F. The effect of thermal treatment on the stress state and evolving microstructure of Cu/W nano-multilayers. *J. Appl. Phys.* **2016**, DOI: 10.1063/1.4967992.
- (8) Druzhinin, A. V.; Ariosa, D.; Siol, S.; Ott, N.; Straumal, B. B.; Janczak-Rusch, J.; Jeurgens, L. P. H.; Cancellieri, C. Effect of the individual layer thickness on the transformation of Cu/W nano-multilayers into nanocomposites. *Materialia* **2019**, *7*, 100400.
- (9) Moszner, F.; Cancellieri, C.; Chiodi, M.; Yoon, S.; Ariosa, D.; Janczak-Rusch, J.; Jeurgens, L. P. H. Thermal stability of Cu/W nano-multilayers. *Acta Mater.* **2016**, *107*, 345–353.
- (10) Druzhinin, A. V.; Rheingans, B.; Siol, S.; Straumal, B. B.; Janczak-Rusch, J.; Jeurgens, L. P. H.; Cancellieri, C. Effect of internal stress on short-circuit diffusion in thin films and nanolaminates: Application to Cu/W nano-multilayers. *Appl. Surf. Sci.* **2020**, *508*, 145254.
- (11) Raghavan, R.; Wheeler, J. M.; Esqué-De los Ojos, D.; Thomas, K.; Almandoz, E.; Fuentes, G. G.; Michler, J. Mechanical behavior of Cu/TiN multilayers at ambient and elevated temperatures: Stress-assisted diffusion of Cu. *Mater. Sci. Eng., A* **2015**, *620*, 375–382.
- (12) Snel, J.; Monclús, M. A.; Castillo-Rodríguez, M.; Mara, N.; Beyerlein, I. J.; Llorca, J.; Molina-Aldareguía, J. M. Deformation Mechanism Map of Cu/Nb Nanoscale Metallic Multilayers as a Function of Temperature and Layer Thickness. *JOM* **2017**, *69*, 2214–2226.
- (13) Tishkevich, D. I.; Grabchikov, S. S.; Tsybulska, L. S.; Shendyukov, V. S.; Perevoznikov, S. S.; Trukhanov, S. V.; Trukhanova, E. L.; Trukhanov, A. V.; Vinnik, D. A. Electrochemical

deposition regimes and critical influence of organic additives on the structure of Bi films. *J. Alloys Compd.* **2018**, 735, 1943–1948.

(14) Tishkevich, D. I.; Grabchikov, S. S.; Lastovskii, S. B.; Trukhanov, S. V.; Zubar, T. I.; Vasin, D. S.; Trukhanov, A. V. Correlation of the synthesis conditions and microstructure for Bi-based electron shields production. *J. Alloys Compd.* **2018**, 749, 1036–1042.

(15) Zubar, T. I.; Fedosyuk, V. M.; Trukhanov, S. V.; Tishkevich, D. I.; Michels, D.; Lyakhov, D.; Trukhanov, A. V. Method of surface energy investigation by lateral AFM: application to control growth mechanism of nanostructured NiFe films. *Sci. Rep.* **2020**, 10, 1–10.

(16) Zubar, T.; Fedosyuk, V.; Tishkevich, D.; Kanafyev, O.; Astapovich, K.; Kozlovskiy, A.; Zdorovets, M.; Vinnik, D.; Gudkova, S.; Kaniukov, E.; Sombra, A. S. B.; Zhou, D.; Jotania, R. B.; Singh, C.; Trukhanov, S.; Trukhanov, A. The Effect of Heat Treatment on the Microstructure and Mechanical Properties of 2D Nanostructured Au/NiFe System. *Nanomaterials* **2020**, 10, 1077.

(17) Brandt, L. R.; Salvati, E.; Papadaki, C.; Zhang, H.; Ying, S.; Le Bourhis, E.; Dolbnya, I.; Sui, T.; Korsunsky, A. M. Probing the deformation and fracture properties of Cu/W nano-multilayers by in situ SEM and synchrotron XRD strain microscopy. *Surf. Coat. Technol.* **2017**, 320, 158–167.

(18) Björck, M.; Andersson, G. GenX: an extensible X-ray reflectivity refinement program utilizing differential evolution. *J. Appl. Crystallogr.* **2007**, 40, 1174–1178.

(19) Filik, J.; Ashton, A. W.; Chang, P. C. Y.; Chater, P. A.; Day, S. J.; Drakopoulos, M.; Gerring, M. W.; Hart, M. L.; Magdysyuk, O. V.; Michalik, S.; Smith, A.; Tang, C. C.; Terrill, N. J.; Wharmby, M. T.; Wilhelm, H. Processing two-dimensional X-ray diffraction and small-angle scattering data in DAWN 2. *J. Appl. Crystallogr.* **2017**, 50, 959–966.

(20) Müller-Buschbaum, P. Grazing incidence small-angle X-ray scattering: An advanced scattering technique for the investigation of nanostructured polymer films. *Anal. Bioanal. Chem.* **2003**, 376, 3–10.

(21) Pospelov, G.; Van Herck, W.; Burle, J.; Loaiza, J. M. C.; Durniak, C.; Fisher, J. M.; Ganeva, M.; Yurov, D.; Wuttke, J. BornAgain: Software for simulating and fitting grazing-incidence small-angle scattering. *J. Appl. Crystallogr.* **2020**, 53, 262–276.

(22) BornAgain — Software for simulating and fitting X-ray and neutron small-angle scattering at grazing incidence, 2020; <https://www.bornagainproject.org>.

(23) Profilmonline, (n.d.). <https://www.profilmonline.com/> (accessed 2020-10-06).

(24) Czigány, Z.; Radnóczy, G. Columnar growth structure and evolution of wavy interface morphology in amorphous and polycrystalline multilayered thin films. *Thin Solid Films* **1999**, 347, 133–145.

(25) Romano Brandt, L.; Reza, A.; Salvati, E.; Le Bourhis, E.; Hofmann, F.; Korsunsky, A. M. Controlling Thermal Diffusivity, Residual Stress and Texture in W/Cu Nano-Multilayers by Magnetron Chamber Pressure Variation. *SSRN Electron. J.* **2020**, DOI: 10.2139/ssrn.3708733.

(26) Bundesmann, C.; Neumann, H. Tutorial: The systematics of ion beam sputtering for deposition of thin films with tailored properties. *J. Appl. Phys.* **2018**, 124, 231102.

(27) Osetskyy, Y. N.; Bacon, D. J.; Serra, A.; Singh, B. N.; Golubov, S. I. One-dimensional atomic transport by clusters of self-interstitial atoms in iron and copper. *Philos. Mag.* **2003**, 83, 61–91.

(28) Gilmore, C. M.; Sprague, J. A. Molecular dynamics simulation of defect formation during energetic Cu deposition. *Thin Solid Films* **2002**, 419, 18–26.

(29) Windischmann, H. Intrinsic stress in sputter-deposited thin films. *Crit. Rev. Solid State Mater. Sci.* **1992**, 17, 547–596.

(30) Magnfält, D.; Abadias, G.; Sarakinos, K. Atom insertion into grain boundaries and stress generation in physically vapor deposited films. *Appl. Phys. Lett.* **2013**, 103, 051910.

(31) Girault, B. Étude De L'Effet De Taille Et De Structure Sur L'Elasticité, Thesis, 2008.

(32) Yang, J.; Deng, W.; Li, Q.; Li, X.; Liang, A.; Su, Y.; Guan, S.; Wang, J.; He, D. Strength enhancement of nanocrystalline tungsten under high pressure. *Matter Radiat. Extrem.* **2020**, 5, 058401.

(33) Romano-Brandt, L.; Salvati, E.; Le Bourhis, E.; Moxham, T.; Dolbnya, I. P.; Korsunsky, A. M. Nano-scale residual stress depth profiling in Cu/W nano-multilayers as a function of magnetron sputtering pressure. *Surf. Coat. Technol.* **2020**, 381, 125142.

(34) Foote, F.; Jette, E. R. The fundamental relation between lattice constants and density. *Phys. Rev.* **1940**, 58, 81–86.

(35) Chason, E.; Mayer, T. M. Thin film and surface characterization by specular X-ray reflectivity. *Crit. Rev. Solid State Mater. Sci.* **1997**, 22, 1–67.

(36) Bockstedte, M.; Mattausch, A.; Pankratov, O. Ab initio study of the annealing of vacancies and interstitials in cubic SiC: Vacancy-interstitial recombination and aggregation of carbon interstitials. *Phys. Rev. B: Condens. Matter Mater. Phys.* **2004**, 69, 235202.

(37) Dienes, G. J.; Damask, A. C. Kinetics of vacancy-interstitial annihilation. III. Interstitial migration to sinks. *Phys. Rev.* **1962**, 128, 2542–2546.

(38) Zhao, J. H.; Du, Y.; Morgen, M.; Ho, P. S. Simultaneous measurement of Young's modulus, poisson ratio, and coefficient of thermal expansion of thin films on substrates. *J. Appl. Phys.* **2000**, 87, 1575–1577.

(39) Lahav, A.; Grim, K. A.; Blech, I. A. Measurement of thermal expansion coefficients of W, WSi, WN, and WSiN thin film metallizations. *J. Appl. Phys.* **1990**, 67, 734–738.

(40) Janczak-Rusch, J.; Chiodi, M.; Cancellieri, C.; Moszner, F.; Hauert, R.; Pigozzi, G.; Jeurgens, L. P. H. Structural evolution of Ag-Cu nano-alloys confined between AlN nano-layers upon fast heating. *Phys. Chem. Chem. Phys.* **2015**, 17, 28228–28238.

(41) Jiang, H.; Hua, W.; Tian, N.; Li, A.; Li, X.; He, Y.; Zhang, Z. In situ GISAXS study on the temperature-dependent performance of multilayer monochromators from the liquid nitrogen cooling temperature to 600 °C. *Appl. Surf. Sci.* **2020**, 508, 144838.

(42) Horváth, J.; Birringer, R.; Gleiter, H. Diffusion in nanocrystalline material. *Solid State Commun.* **1987**, 62, 319–322.

(43) Solberg, J. K. The crystal structure of  $\eta$ -Cu<sub>3</sub>Si precipitates in silicon. *Acta Crystallogr., Sect. A: Cryst. Phys., Diff., Theor. Gen. Crystallogr.* **1978**, 34, 684–698.

(44) Ponweiser, N.; Richter, K. W. New investigation of phase equilibria in the system Al-Cu-Si. *J. Alloys Compd.* **2012**, 512, 252–263.

(45) Seibt, M.; Griess, M.; Istratov, A. A.; Hedemann, H.; Sattler, A.; Schröter, W. Formation and properties of copper silicide precipitates in silicon. *Phys. Status Solidi Appl. Res.* **1998**, 166, 171–182.

(46) Salem, M. M.; Panina, L. V.; Trukhanova, E. L.; Darwish, M. A.; Morchenko, A. T.; Zubar, T. I.; Trukhanov, S. V.; Trukhanov, A. V. Structural, electric and magnetic properties of (BaFe<sub>11.9</sub>Al<sub>0.1</sub>O<sub>19</sub>)<sub>1-x</sub> - (BaTiO<sub>3</sub>)<sub>x</sub> composites, *Compos. Composites, Part B* **2019**, 174, 107054.

(47) Kozlovskiy, A. L.; Zdorovets, M. V. The study of the structural characteristics and catalytic activity of Co/CoCo<sub>2</sub>O<sub>4</sub> nanowires. *Composites, Part B* **2020**, 191, 107968.

(48) Trukhanov, S. V.; Troyanchuk, I. O.; Pushkarev, N. V.; Szymczak, H. The influence of oxygen deficiency on the magnetic and electric properties of La<sub>0.70</sub>Ba<sub>0.30</sub>MnO<sub>3- $\gamma$</sub>  ( $0 \leq \gamma \leq 0.30$ ) Manganite with a perovskite structure. *J. Exp. Theor. Phys.* **2002**, 95, 308–315.

(49) Zdorovets, M. V.; Kozlovskiy, A. L. The effect of lithium doping on the ferroelectric properties of LST ceramics. *Ceram. Int.* **2020**, 46, 14548–14557.